Article

Ag@SiO$_2$ Core-shell Nanoparticles Embedded in a TiO$_2$ Mesoporous Layer Substantially Improve the Performance of Perovskite Solar Cells

Bao Wang [†], Xiangyu Zhu [†], Shuhan Li, Mengwei Chen, Haifei Lu and Yingping Yang *

School of Science, Wuhan University of Technology, Wuhan 430070, China; 1174828021@whut.edu.cn (B.W.); zxy371653016@whut.edu.cn (X.Z.); 204410@whut.edu.cn (S.L.); mengwei.chen@whut.edu.cn (M.C.); haifeilv@whut.edu.cn (H.L.)

* Correspondence: ypyang@whut.edu.cn; Tel.: +86-27-8710-8039

† These authors contributed equally to this work.

check for updates

Abstract: In this study, Ag@SiO$_2$ nanoparticles were synthesized by a modified Stöber method for preparing the TiO$_2$ mesoporous layer of carbon counter electrode-based perovskite solar cells (PSCs) without a hole transporting layer. Compared with normal PSCs (without Ag@SiO$_2$ incorporated in the TiO$_2$ mesoporous layer), PSCs with an optimal content of Ag@SiO$_2$ (0.3 wt. % Ag@SiO$_2$-TiO$_2$) show a 19.46% increase in their power conversion efficiency, from 12.23% to 14.61%, which is mainly attributed to the 13.89% enhancement of the short-circuit current density, from 20.23 mA/cm^2 to 23.04 mA/cm^2. These enhancements mainly contributed to the localized surface Plasmon resonance effect and the strong scattering effect of Ag@SiO$_2$ nanoparticles. However, increasing the Ag@SiO$_2$ concentration in the mesoporous layer past the optimum level cannot further increase the short-circuit current density and incident photon-to-electron conversion efficiency of the devices, which is primarily ascribed to the electron transport pathways being impeded by the insulating silica shells inside the TiO$_2$ network.

Keywords: Ag@SiO$_2$ nanoparticles; perovskite solar cell; localized surface Plasmon resonance effect; scattering effect

1. Introduction

Over the past few years, much significant progress has been made in the development of perovskite solar cells (PSCs), such as the low-cost but high-efficiency CuSCN replacing spiro-OMeTAD [1], breakthroughs in large-area perovskite films fabrication [2] and constant improvements in power conversion efficiencies (PCEs), from an initial 3.9% to 23.2% [3,4]. Due to the excellent photovoltaic properties of perovskite, such as large light-harvesting coefficient, long carrier diffusion distance and high carrier mobility [5–9], PSCs have a bright prospect of partly replacing conventional energy. Recently, Bella et al. [10] made a 360-degree overview focusing on Cs-doping for PSCs to illustrate the excellent properties of Cs in perovskite-based devices. Bella et al. [11] explained the different electrochemical behavior of the amorphous and anatase phases of TiO2 and clarified the controversial mechanism of reversible Na storage in TiO$_2$ nanotube arrays. Zhang et al. [12] prepared TiO2@C aerogel as superior anode for lithium-ion batteries which exhibited a superior high rate and stable performance. Bella et al. [13] introduced the photoanodes and cathodes exclusively based on polymeric materials into dye-sensitized solar cells (DSSCs) and obtained a 5.33% power conversion efficiency. Galliano et al. [14] made a multivariate study on aqueous DSSCs to provide a new approach of finding the optimal operating conditions of any new energy device with solid mathematical and

statistical bases. Abate et al. [15] analyzed the critical points about currently limiting the industrial production of PSCs.

However, being high efficient light harvesters, the thickness of organo-metal halide perovskites should be limited, reducing the lead content as much as possible, due to environmental and health concerns [16,17]. Therefore, the light capture capability of perovskite absorbers (PA) must be appropriately regulated to reach optimum efficiency. One strategy to improve the utilization rate of sunlight of PA could be incorporating metal nanoparticles (NPs) into PSCs.

When the photon frequency matches the natural oscillation frequency of the metal NP surface electrons, the conduction band (CB) electrons of noble metal NPs are induced to the coherent surface Plasmon oscillations [18], which is termed localized surface Plasmon resonance (LSPR). Consequently, this causes a huge increase in light absorption and scattering [19,20]. LSPR is macroscopically expressed as a strong characteristic absorption peak in the ultraviolet-visible (UV-vis) absorption spectrum. Mixing metal NPs into PSCs could not only enhance the optical properties related to size, shape, structure and environment [21] but also make use of electrical characteristics which are reported to help dissociate excitons and transport carriers more efficiently [22].

Certainly, there are numerous academic papers on the incorporation of metal nanomaterials into photovoltaic devices for better performance via their optical and electrical properties [23–25]. For example, Wang et al. [26] significantly improved the PCEs by adding 70 nm-Au NPs into polymer bulk heterojunction solar cells. Kulkarni et al. [27] utilized photoinduced absorption spectroscopy to improve the generation of charge carrier by using silver nanoprisms in organic photovoltaic devices. Batmunkh et al. [28] introduced the plasmonic Au nanostars into PSCs for enhancing photon absorption and thus improving device performance. Furthermore, an insulating SiO_2 shell was added onto the surface of metal NPs to inhibit corrosion [29] and exciton quenching [30], however, this did not influence the LSPR effect. Metal-oxide core-shell NPs have widespread application in PSCs [31–36], as well as in DSSCs [37] and organic solar cells [38,39]. However, there has been little research on incorporating $Ag@SiO_2$ NPs into low-cost free-hole-conductor PSCs with carbon counter electrodes. Ag NPs show superior scattering efficiency compared to any other metal NPs [40].

In this work, we adopted a modified Stöber [41] method to prepare $Ag@SiO_2$ NPs for manufacturing the TiO_2 mesoporous layer of PSCs. Through ultrasound treatment and continuous stirring, $Ag@SiO_2$ NPs and mesoporous TiO_2 pulp suspension were thoroughly homogenized. PSCs with $Ag@SiO_2$ NPs exhibited better performance, evidenced by their UV-vis absorption spectra, *J-V* curves and incident photon-to-electron conversion efficiency (IPCE) spectra, because of the strong LSPR and scattering effects. With the hole-conductor-free and carbon-based counter electrode, the PSC devices gained a 19.46% enhancement of PCE, from 12.23% to 14.61% and a 13.89% increase in short-circuit current density (J_{SC}), from 20.23 mA/cm^2 to 23.04 mA/cm^2.

2. Results and Discussion

We successfully synthesized Ag NPs with a polyol method, whereas the silica shells coated on the Ag NPs were deposited uniformly with a modified Stöber method. The obtained NPs were then characterized by field emission transmission electron microscopy (FE-TEM, JEOL Ldt., Tokyo, Japan), high-resolution TEM (HRTEM, JEOL Ldt., Tokyo, Japan) and UV-vis absorption spectra (UV3600, Shimadzu Corporation, Tokyo, Japan). As depicted in Figure 1a, Ag NPs were evenly dispersed in ethanol, with the size distribution results in the upper right corner of the image. The nucleation sizes of the Ag NPs were almost equal and basically concentrated at 26 nm, while the thickness of the silica shells averaged 14 nm. Figure 1b shows the HRTEM image of a $Ag@SiO_2$ NP. The lattice fringes of the Ag NP can be observed and were measured at about 2.40 Å matched with the (111) crystallographic planes of Ag NPs, which is consistent with the available literature [42].
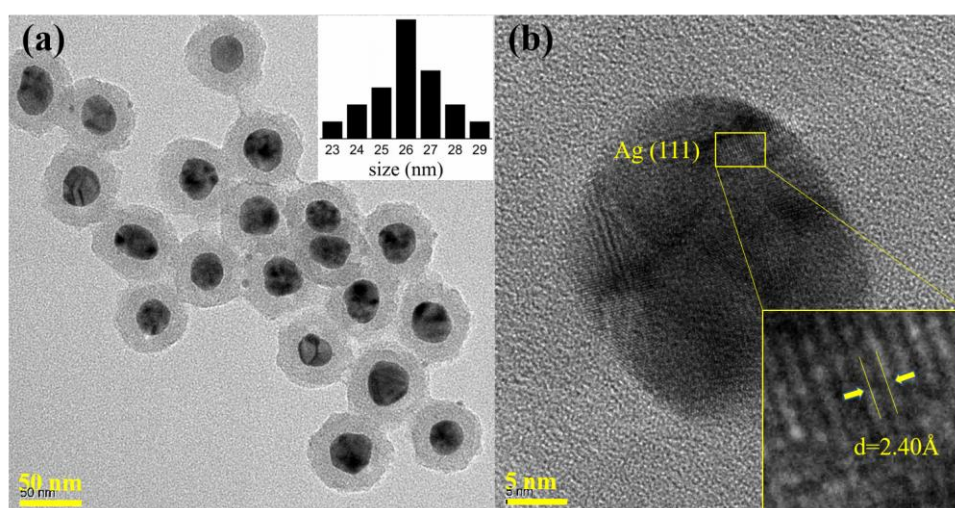
Figure 1. (**a**) TEM image and size distribution results of Ag@SiO$_2$ NPs; (**b**) HRTEM image of a Ag@SiO$_2$ NP.

Figure 2a shows the X-ray diffraction (XRD) patterns of mesoporous TiO$_2$ and the mesoporous TiO$_2$ mixed with Ag@SiO$_2$ NPs. A series of matching diffraction peaks characteristic for TiO$_2$ were observed at 25°, 38°, 48°, 54°, 55°, 63°, 69°, 70°, 75°, 83°, which correspond to the anatase phase according to the standard PDF card (JCPDS Card No. 89-4921). These characteristic diffraction peaks are respectively attributed to the (101), (004), (200), (105), (211), (204), (116), (220), (215), (224) crystal planes of anatase phase TiO$_2$. Simultaneously, there are several additional diffraction peaks in Figure 2a at the angles of 38°, 44°, 65° and 78°; these correspond to the reflections of the (111), (200), (220) and (311) crystal planes of the Ag NPs [43]. Furthermore, no other characteristic diffraction peaks of Ag oxide and SiO$_2$ were observed, which implies that Ag was present in crystal form and SiO$_2$ in an amorphous state in the prepared samples. Figure 2b exhibits the optical absorption spectra of 26 nm-Ag NPs and Ag@SiO$_2$ NPs dispersed in alcohol solution. Compared to Ag NPs, the Plasmon resonance peak of Ag@SiO$_2$ NPs had an obvious red-shift of around 10 nm, which was caused by the large refractive index of the silica shell [44,45]. The red-shifted distances of Ag@SiO$_2$ NPs are related to the thickness of the silica shells, which are relative to the added amount of ethylsilicate [46]. The dielectric SiO$_2$ shells coated around Ag NPs could prevent the recombination of carriers on the surface of metal NPs [30], even further enhancing the LSPR effect [47], as already reported.
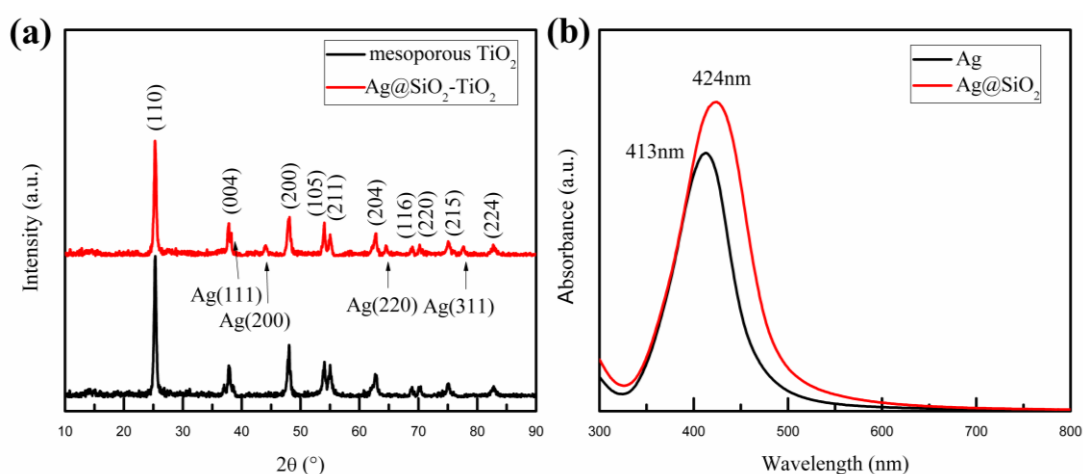
Figure 2. (**a**) XRD patterns of mesoporous TiO$_2$ and the Ag@SiO$_2$-TiO$_2$; (**b**) Optical absorption spectra of 26 nm-Ag NPs and Ag@SiO$_2$ NPs dispersed in alcohol.

To confirm the physical state of chemical elements in the mesoporous TiO_2 mixed with $Ag@SiO_2$ NPs, X-ray photoelectron spectroscopy (XPS) was performed to assess the binding energy of chemical elements in the sample. Figure 3 shows the Ti, O, Si, Ag binding states and the surface composition of the NPs. As pictured in Figure 3a,b, the binding energies of 457.2 eV, 463.0 eV and 528.9 eV, correspond to the peaks of Ti $2p_{3/2}$, Ti $2p_{1/2}$ and O 1s respectively. However, compared with the pristine TiO_2, the binding energies of the Ti $2p_{3/2}$, Ti $2p_{1/2}$ and O 1s electrons increased to 0.6 eV, 0.6 eV and 0.4 eV, respectively, after the addition of $Ag@SiO_2$ NPs, which implies that a few electrons of the Ti and O atoms were trapped by $Ag@SiO_2$ NPs due to the local electromagnetic field [48]. The decrease in electrons around Ti and O atoms implies a reduction in electron cloud densities around the Ti and O atoms and thus an increase in the binding energies. Figure 3c shows the peak of Si 2p at the binding energy of 103 eV, which is in accord with the standard database. In Figure 3d, no distinct peak can be found, which suggests that the 10 nm silica shells around the Ag NPs are sufficiently thick to attenuate the Ag photoelectrons generated by the X-ray [49]. Nonetheless, after a simple smoothing treatment, a weak peak was observed at the binding energy of 367 eV, corresponding to the peak of Ag $3d_{5/2}$. Compared with the standard binding energy of Ag^0 at 368.25 eV, there is a small decrease that may be attributed to the few Ag NPs not covered by the silica shells. While calcinating the samples, the increased temperature led to the growth of the Ag NPs, which decreased the Ag $3d_{5/2}$ electronic binding energy [48]. Both the XRD patterns and XPS survey spectra indicate that the $Ag@SiO_2$ NPs were successfully mixed into the TiO_2 mesoporous layer.
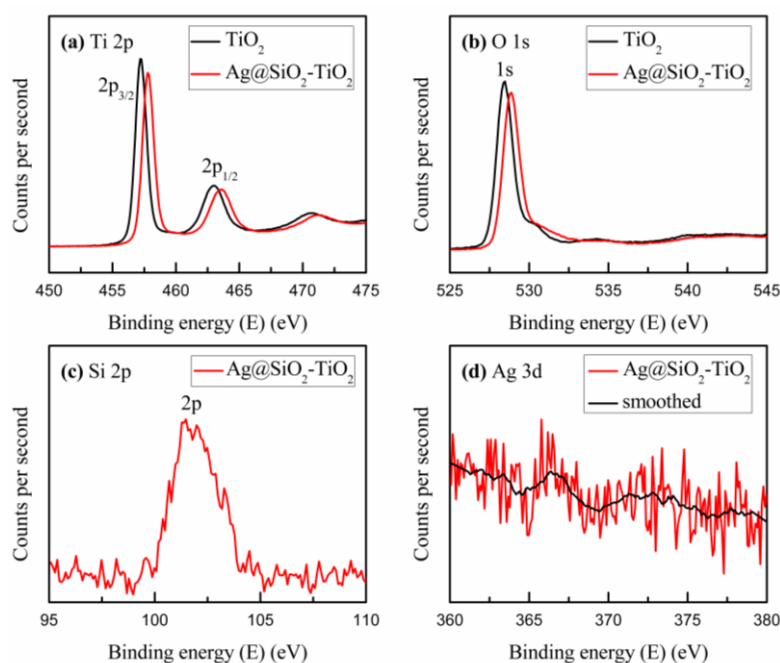
Figure 3. XPS survey spectra acquired from mesoporous TiO_2 and the $Ag@SiO_2$-TiO_2: (**a**) Ti 2p; (**b**) O 1s; (**c**) Si 2p; (**d**) Ag 3d.

As depicted in Figure 4, a whole PSC device includes glass, FTO, a TiO_2 compact layer, TiO_2 mesoporous layer, ZrO_2 mesoporous layer, perovskite layer and carbon counter electrode from the bottom up. According to the scale plate in Figure 4a, the thickness of each layer of the solar cell could be diagrammatically calculated. The thickness of the FTO, TiO_2 compact layer, TiO_2 mesoporous layer/perovskite and ZrO_2 mesoporous layer/perovskite was roughly 500 nm, 30 nm 100 nm and 100 nm, respectively. In addition, the carbon counter electrode film was almost 30 μm, which is upon the perovskite film by screen printing. In the FTO/c-TiO_2/m-TiO_2/m-ZrO_2/perovskite/carbon architecture-based PCSs, the ZrO_2 layer acting as a scaffold to host the perovskite absorber with TiO_2

layer, can block the flow of photogenerated electrons to the back contact and prevent recombination with the holes from the perovskite at the back contact [50].
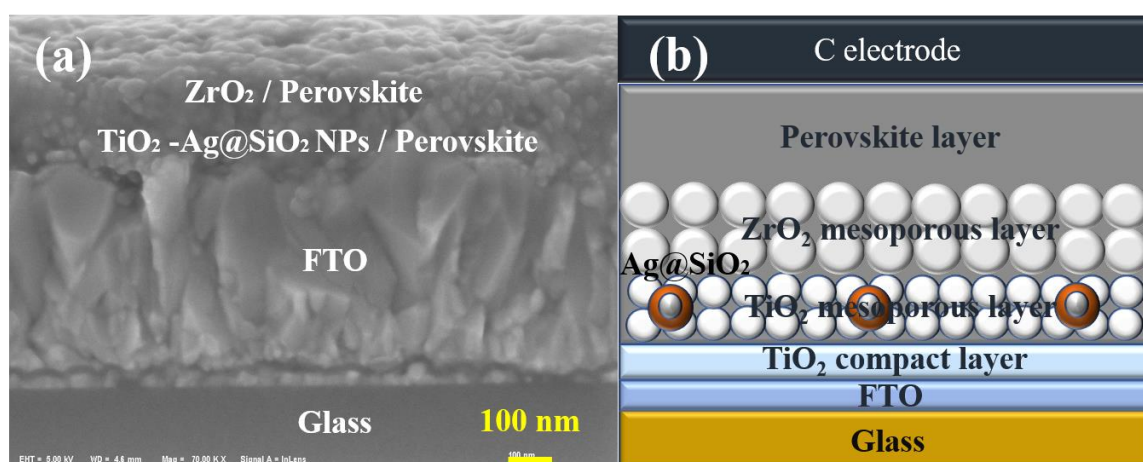
Figure 4. (**a**) Scanning Electron Microscope (SEM) image of a cross section of a complete PSC mixed with Ag@SiO$_2$ NPs; (**b**) Structural representation of a whole PSC device mixed with Ag@SiO$_2$ NPs.

The UV-vis absorption spectra of pristine TiO$_2$ and TiO$_2$ mixed with Ag@SiO$_2$ NPs mesoporous film samples are presented in Figure 5a. The black absorption curve represents the absorption intensity of pristine mesoporous TiO$_2$ in the wavelength of 300–800 nm, which has an absorption peak at approximately 325 nm and is nearly zero in 360–800 nm, as previously reported by Yue et al. [51]. Compared with the other absorption curves, it is evident that the intensity of the absorption peak at around 325 nm became stronger as the content of Ag@SiO$_2$ NPs in the mesoporous TiO$_2$ layer gradually increased. As pictured in Figure 5b, the UV-vis absorption spectra of PSCs with pristine TiO$_2$ and TiO$_2$ mixed with Ag@SiO$_2$ NPs followed the same trend in Figure 5a. The enhancement could be attributed to the LSPR effect and scattering effect of Ag@SiO$_2$ NPs. By absorbing photons in the wavelength of the plasmonic resonance band, Ag@SiO$_2$ NPs produced an intense LSPR effect which stimulated a strong electromagnetic field [52]. The intense local electromagnetic field could cause bandgap excitation for the nearby TiO$_2$ NPs, enhancing their photocatalytic abilities, which could generate more electron-hole pairs in the TiO$_2$ NPs [53]. The scattering effect of Ag@SiO$_2$ NPs is mainly due to the scattering of incident light by the Ag NPs, which increases the length of the light propagation path and then further improves light trapping and the light utilization rate [34]. Macroscopically, the LSPR and scattering effects of Ag@SiO$_2$ NPs are shown in the absorption spectrum, as depicted in Figure 5. As the content of Ag@SiO$_2$ NPs increases, the LSPR effect and scattering effect increase gradually, which correlates with the absorption curves. According to previous research, the LSPR effect and scattering effect are dependent on the size of the metal NPs, with the LSPR effect decreasing as the metal NPs grow and the scattering effect increasing as the metal NPs grow [21,40]. Based on Zhang's calculations, for Ag NPs, the LSPR effect reaches the maximum absorption efficiency at 20 nm, while the scattering effect achieves maximum scattering efficiency at 40 nm [54]. For the relatively small 26 nm-Ag NPs, the LSPR effect plays a more significant role than the scattering effect in the PSC devices [40,54].
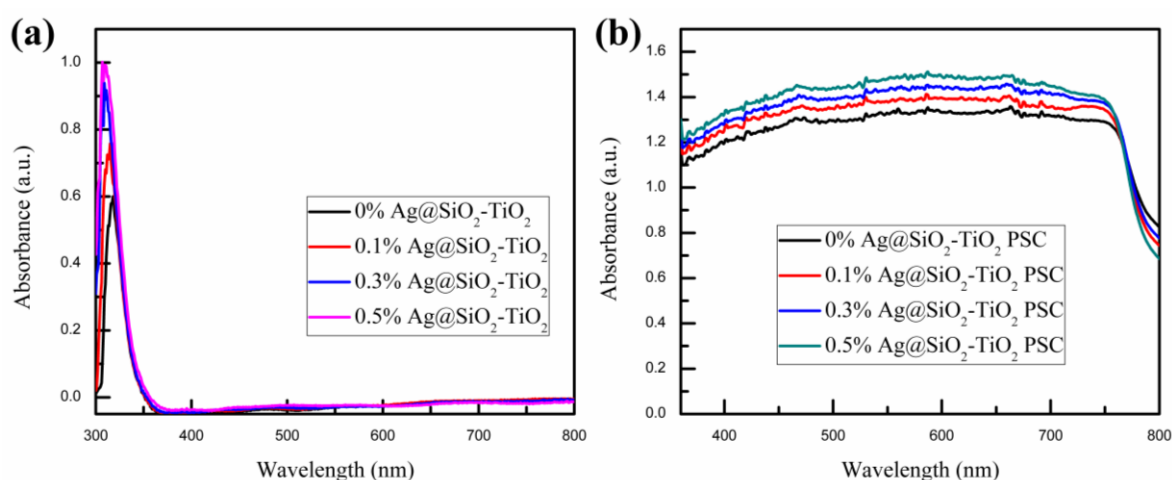
Figure 5. UV-vis absorption spectra of (**a**) pristine TiO_2 and TiO_2 mixed with Ag@SiO_2 NPs mesoporous film samples and (**b**) PSCs with pristine TiO_2 and TiO_2 mixed with Ag@SiO_2 NPs mesoporous film.

The PSCs based on mesoporous TiO_2 film mixed with different amounts of Ag@SiO_2 NPs were measured via scanning from -1.1 V to short circuit at a scan rate of 150 mV/s under AM 1.5G irradiation (100 mW/cm^2) in ambient air to characterize their photovoltaic performance. Except for the process of spin-coating the perovskite solution, which was accomplished inside a nitrogen glovebox, all other processes, including spin-coating the precursor solution of the compact TiO_2 layer, spin-coating the pulp suspension of mesoporous TiO_2 mixed with different amounts of Ag@SiO_2 NPs and mesoporous ZrO_2 and screen-printing the carbon counter electrode, were performed in ambient air, at room temperature. As shown in Figure 6a, the PSC devices containing 0.3 wt. % Ag@SiO_2 NPs had the most outstanding photovoltaic performance. Summarized photovoltaic parameters of PSCs based on mesoporous TiO_2 film mixed with different amounts of Ag@SiO_2 NPs are described in Table 1, which corresponds to Figure 6a. Figure 7 shows the histograms of photovoltaic parameters for 12 devices (the same batch of samples) based on mesoporous TiO_2 film mixed with 0.3 wt. % Ag@SiO_2 NPs. Compared with normal PSCs (with no plasmonic NPs), the photovoltaic performance of cells containing 0.3 wt. % Ag@SiO_2 NPs was enhanced 19.46% regarding their PCE (from 12.23% to 14.61%) and 13.89% at J_{SC}, from 20.23 mA/cm^2 to 23.04 mA/cm^2, while the open-circuit voltages (V_{OC}) and fill factor (FF) of the PSCs rose and fell slightly at 1.00 V and 61.00%, respectively. The enhancements could be attributed to the incorporation of Ag@SiO_2 NPs, which generated strong LSPR and scattering effects, improving the light trapping and utilization rate. The V_{OC} of the PSC devices are related to the CBs of TiO_2 and perovskite [55] and were not influenced by the Ag@SiO_2 NPs. As described in Figure 6a and Table 1, as the number of Ag@SiO_2 NPs increased gradually, the J_{SC} and PCE initially increased, reaching the optimal value with the addition of 0.3 wt. % Ag@SiO_2 NPs and then decreased. The enhancement was due to the strong increase in LSPR effect and scattering effect, while the diminution may be attributed to the offset between plasmonic light trapping effects and the decrease in electron transmission routes with the increased Ag@SiO_2 loading [56]. Certainly, PSCs usually suffer from a hysteresis effect in *J-V* measurements, which is related with measurement settings and device properties [57–59]. In the FTO/c-TiO_2/m-TiO_2/m-ZrO_2/perovskite/carbon architecture-based PCSs, the properties of the c-TiO_2 layer and corresponding interfaces significantly affect the *J-V* hysteresis [60]. As depicted in Figure 6b and Table 2, the photocurrent, voltage, efficiency and fill factor for the forward-reverse scan were a little higher than those for the reverse-forward scan, which indicated that the hysteresis effect was a little influence in this architecture.
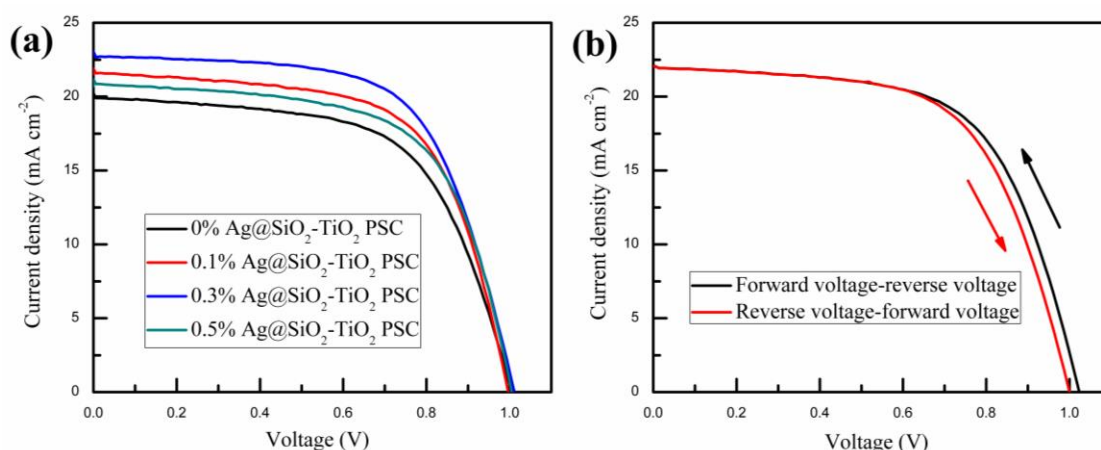
Figure 6. (**a**) *J-V* curves of PSC devices based on mesoporous TiO_2 film mixed with different amounts of Ag@SiO_2 NPs; (**b**) *J-V* curves scanned form forward voltage to reverse voltage and scanned form reverse voltage to forward voltage.

Table 1. Summarized photovoltaic parameters of PSC devices based on mesoporous TiO_2 film mixed with different amounts of Ag@SiO_2 NPs.

Samples	V_{OC} (V)	J_{SC} (mA/cm^2)	PCE (%)	FF (%)
0% Ag@SiO_2-TiO_2	1.00	20.23	12.23	60.45
0.1% Ag@SiO_2-TiO_2	0.99	21.90	13.65	62.96
0.3% Ag@SiO_2-TiO_2	1.02	23.04	14.61	62.17
0.5% Ag@SiO_2-TiO_2	0.99	21.16	13.20	63.01
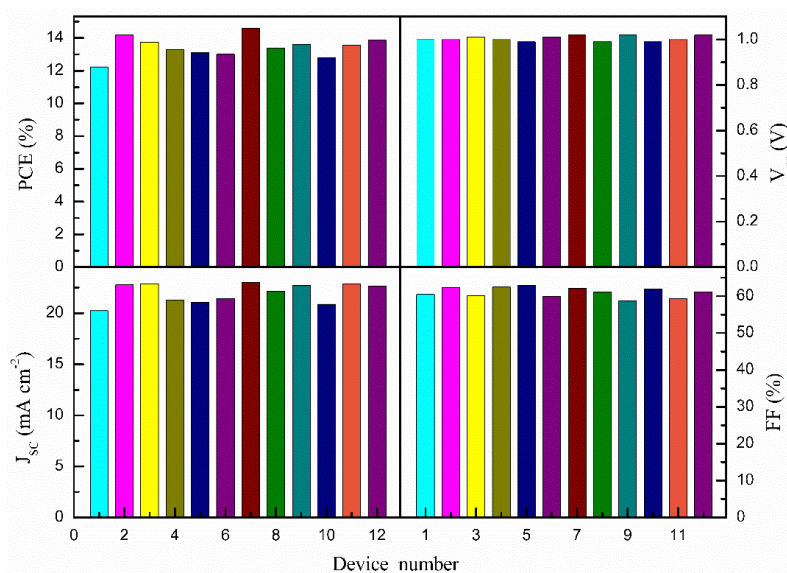
Figure 7. Histograms of photovoltaic parameters for 12 devices (the same batch of samples) based on mesoporous TiO_2 film mixed with 0.3 wt. % Ag@SiO_2 NPs.

Table 2. Summarized photovoltaic parameters of PSC devices scanned form forward voltage to reverse voltage and scanned form reverse voltage to forward voltage.

Samples	V_{OC} (V)	J_{SC} (mA/cm^2)	PCE (%)	FF (%)
Forward-reverse	1.02	22.23	13.88	61.21
Reverse- forward	1.00	22.22	13.50	60.76

The IPCE spectra of PSC devices were measured to further demonstrate the impact of Ag@SiO$_2$ NPs on the photoelectric properties of PSCs. It is evident that the trends shown in Figure 8 were consistent with the *J-V* curves depicted in Figure 6. With increased loading of Ag@SiO$_2$ NPs, the IPCE reached its maximum at the concentration of 0.3 wt. %, followed by a decrease as the Ag@SiO$_2$ NPs content increased past the optimal value. As pictured in Figure 8, in the wavelength of 500–750 nm, substantial increases were observed compared to the reference device (the black curve). This may be attributed to the perovskite material, which can efficiently use light in the short wavelength but behaves relatively poor in the long wavelength region of 600–800 nm [61,62]. Therefore, the LSPR effect and scattering effect of Ag@SiO$_2$ NPs performed relatively better in the long wavelength. According to previous research, it is crucial to obtain the electron transport paths simple, straight and with few crystal boundaries to collect more electrons [63,64]. However, with increased concentration of Ag@SiO$_2$ NPs, electrons became impeded by the insulating silica shells on the way to the electrode inside the TiO$_2$ network [56]. Hence, as the Ag@SiO$_2$ concentration increased past the optimal value, the J_{SC} and IPCE curves presented a downward trend.
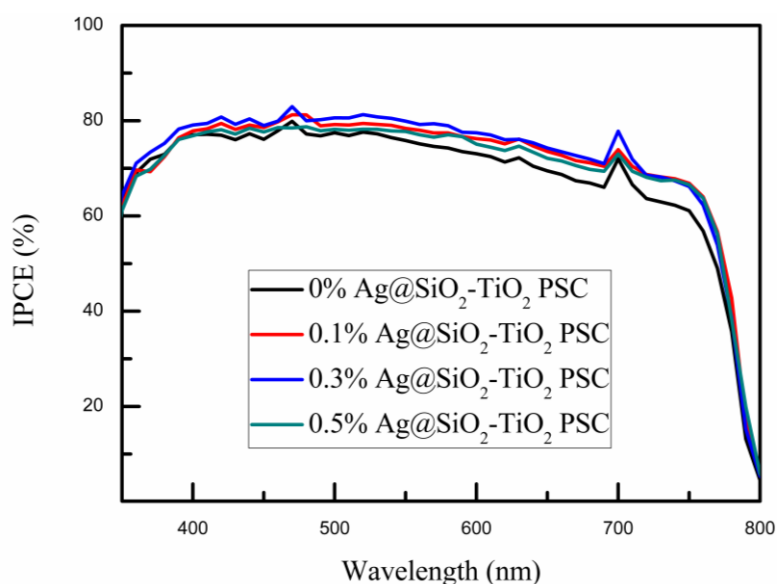
Figure 8. IPCE spectra of PSC devices based on mesoporous TiO$_2$ film mixed with different amounts of Ag@SiO$_2$ NPs.

To understand the charge transport properties of the devices in more details, we studied the photoluminescence (PL) at room temperature of 296 K. In Figure 9, it was obvious that there was a clear quenching of the steady-state PL for the compact TiO$_2$/Ag@SiO$_2$-TiO$_2$/ZrO$_2$/perovskite films compared with the films without Ag@SiO$_2$ NPs, which was contributed from ionization of the excitons and enhanced charge separation [65]. The electrochemical impedance spectroscopy (EIS) analyses were performed for frequencies of 10 mHz to 10 MHz at a bias of 0.8 V under simulated AM 1.5G radiation (irradiance of 100 mW/cm^2) to further understand charge transport and charge recombination in the devices. As described in Figure 10a, there were two semicircles in the Nyquist plots, which corresponded to the high-frequency region and low-frequency region, respectively. The left semicircle represented charge transfer and charge recombination at the perovskite/C electrode interface associated with the charge transfer resistance (R_{tr}), while the right one represented charge transfer and charge recombination at the perovskite/TiO$_2$ interface related to the recombination resistance (R_{rec}) [66,67]. The series resistance (R_S) value is inversely related to FF value [68]. In Table 3, the R$_S$ of 0% Ag@SiO$_2$-TiO$_2$ PSC was slightly larger than the others, which was in keeping with the FF values in Table 1 basically. For the recombination resistance R_{rec} at the perovskite/TiO$_2$ interface, it was clear that with the Ag@SiO$_2$ NPs mixed into the films R_{rec} values decreased immediately, which

indicated that there were more electrons generated duo to the LSPR effect and scattering effect of Ag@SiO$_2$ NPs and sequentially more electrons were recombined at the perovskite/TiO$_2$ interface. To analyze the charge transfer at the perovskite/C electrode interface, the R_{tr} values were shown in Table 3, which decreased as the content of Ag@SiO$_2$ NPs decreased gradually and increased when the concentration was higher than the optimal value. The results of R_{tr} indicated that there were more holes transported to the C electrode and with increased concentration of Ag@SiO$_2$ NPs higher than the optimal value, holes were impeded by the insulating silica shells on the way to the C electrode inside the TiO$_2$/ZrO$_2$ network. Therefore, 0.3% Ag@SiO$_2$-TiO$_2$ PSC got the best photovoltaic properties in this work, in keeping with *J-V* curves and IPCE spectra.
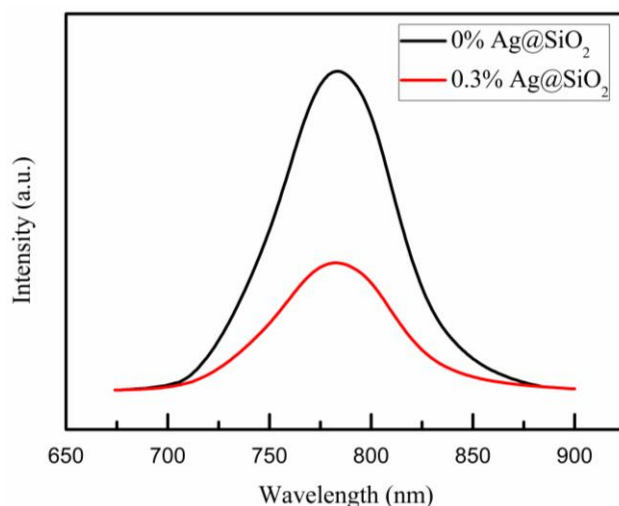
Figure 9. PL spectra of compact TiO$_2$/Ag@SiO$_2$-TiO$_2$/ZrO$_2$/perovskite films at room temperature of 296 K.
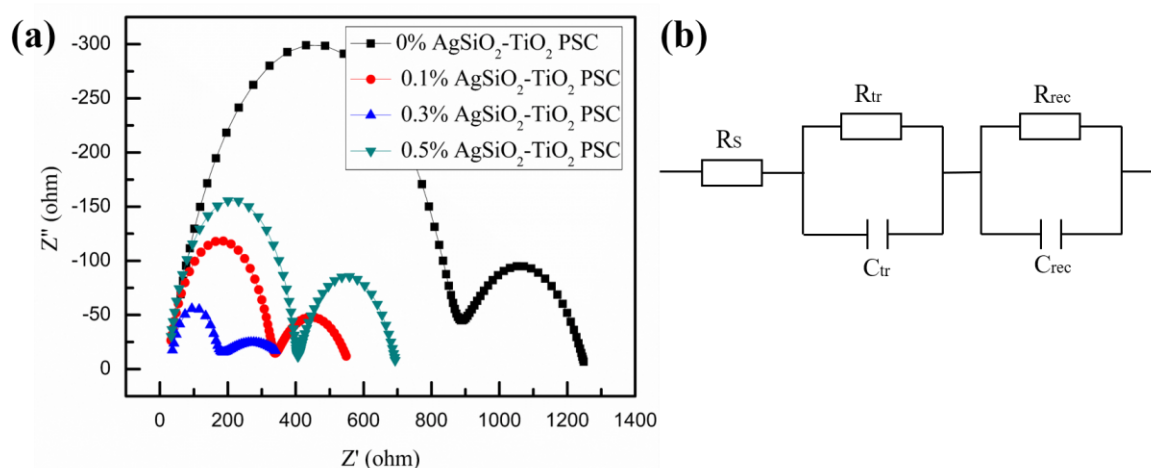
Figure 10. (**a**) Nyquist curves of the PSC devices based on different amounts of Ag@SiO$_2$ NPs films and (**b**) the equivalent circuit employed to fit the plots.

Table 3. Summary of EIS parameters of PSCs based on different amounts of Ag@SiO$_2$ NPs films.

Samples	R_S (Ω)	R_{tr} (Ω)	R_{rec} (Ω)
0% Ag@SiO$_2$-TiO$_2$ PSC	29.75	842.4	381.6
0.1% Ag@SiO$_2$-TiO$_2$ PSC	22.77	308.2	231.1
0.3% Ag@SiO$_2$-TiO$_2$ PSC	25.02	125.8	243.0
0.5% Ag@SiO$_2$-TiO$_2$ PSC	24.84	379.0	294.1

3. Materials and Methods

3.1. Synthesis of Ag NPs

The Ag NPs were prepared *via* a polyol method, according to previously reported methods with slight modifications [40,53,69,70]. First, 3 g polyvinylpyrrolidone (PVP) was dissolved in 40 mL ethylene glycol and heated up to 120 °C slowly, in an oil bath, with continuous stirring, until it dissolved completely. Subsequently, 0.5 g silver nitrate ($AgNO_3$) were dissolved in 20 mL ethylene glycol with vigorous stirring. After the $AgNO_3$ was fully dissolved, the mixture was added to the ethylene glycol solution of PVP dropwise and the resulting solution was kept at 120 °C, for 1 h, under stirring. After the colloidal solution cooled down to room temperature, moderate deionized water was added to the solution, followed by centrifugation. Finally, the precipitate was washed with deionized water and acetone for several times, then dried at 40 °C to obtain the Ag NPs.

3.2. Synthesis of Ag@SiO$_2$ NPs

The Ag@SiO$_2$ NPs were synthesized by a modified Stöber method [40,53,71]. Firstly, 120 mg Ag NPs were uniformly dispersed in 120 mL alcohol with vigorous stirring. Secondly, after 20 min of ultrasonication, 2.5 mL ammonium hydroxide, 2.5 mL deionized water and 0.3 mL ethylsilicate were added to the solution dropwise. Finally, the solution was stirred for 12 h at room temperature and Ag@SiO$_2$ NPs were obtained by centrifugation, wash (ethyl alcohol for several times) and desiccation.

3.3. Device Fabrication

First, to prepare the Ag@SiO$_2$-TiO$_2$ with different ratios (0.1–0.5 wt. %), 4 g alcohol were added to 1 g TiO$_2$ sizing agent (solid content: 20%) followed by stirring for 6 h. Then, 0.2–1 mg Ag@SiO$_2$ NPs powder were added to the mixture followed by stirring for at least 48 h. Normally, Ag@SiO$_2$ NPs disperse in a mixture more uniformly after 30 min of ultrasonication. Second, fluorine-doped tin oxide-patterned glass substrates (7 Ω/sq) were cleaned sequentially with detergent, acetone, isopropanol and ethanol, each followed by 30 min of ultrasonication. Third, the TiO$_2$ compact layer was deposited by spin coating 35 μL TiO$_2$ precursor solution (1 mL titanium disopropoxide bis added into 19 mL ethanol) at 4000 r/min for 25 s and annealed at 150 °C for 10 min. Then, 35 μL TiO$_2$ precursor solution was spin-coated on the substrate again at 4000 r/min for 25 s and annealed at 150 °C for 10 min, followed by annealing at 500 °C for 30 min. Fourth, after cooling down to room temperature, the TiO$_2$ mesoporous layer was deposited on the top of the TiO$_2$ compact layer by spin coating appropriate TiO$_2$ sizing agent mixed with Ag@SiO$_2$ NPs at 3500 r/min for 25 s, after which the glass substrates were heated at 150 °C for 10 min and annealed at 500 °C for 30 min. Fifth, the ZrO$_2$ paste was spun onto the substrates at 5000 r/min for 25 s, then the glass substrates were heated at 150 °C for 10 min and sintered at 500 °C for 30 min. Lastly, the (CH_3NH_3)PbI$_3$ perovskite film was fabricated by spin coating 35 μL perovskite precursor solution at 1000 r/min for 10 s and 4000 r/min for 20 s, followed by annealing at 100 °C for 5–10 min. The perovskite precursor solution was prepared by dissolving 462 mg PbI$_2$ and 178 mg (CH_3NH_3)I in 600 mg dimethylformamide (DMF) and 78 mg dimethyl sulfoxide (DMSO). During 5 s at 4000 r/min, about 200 μL methylbenzene were dropped on the spinning substrates to ensure the fast crystallization of perovskite by extracting the solvent of the perovskite precursor solution.

3.4. Characterization Techniques

FE-TEM images were photographed by a JEM-2100F (JEOL Ldt., Tokyo, Japan). XRD patterns were acquired from an X-ray diffractometer (Advance D8, AXS, Rigaku Corporation, Tokyo, Japan). XPS (ESCALAB 250Xi, Thermo Fisher Scientific, Waltham, Massachusetts, USA) was employed to analyze the chemical elements of the samples. SEM (JSM-IT300, JEOL Ldt., Tokyo, Japan) was used to scan the surface and section of the as-prepared samples. The light-absorption spectra were obtained *via* UV-vis spectrophotometry (UV3600, Shimadzu Corporation, Tokyo, Japan). The photocurrent-voltage

(*J-V*) characteristics were acquired from an electrochemical workstation (Zahner Company, Kronach, Germany) with a solar light simulator (Oriel Sol3A, Newport Corporation, Irvine, CA, USA), under simulated AM 1.5G illumination, at 100 mW/cm^2 intensity. Finally, IPCE (Newport Corporation, Irvine, CA, USA) was employed to study the quantum efficiency of the PSCs. The PL spectra were measured with a fluorescence spectrometer (RF-6000, Shimadzu Corporation, Tokyo, Japan). The EIS analyses were conducted on an electrochemical workstation (Zahner Company, Kronach, Germany) for frequencies of 10 mHz to 10 MHz at a bias of 0.8 V under simulated AM 1.5G radiation (irradiance of 100 mW/cm^2) with an alternating current (AC) signal amplitude of 10 mV at room temperature.

4. Conclusions

In this study, we successfully synthesized Ag@SiO$_2$ NPs with a modified Stöber method and developed PSCs with different contents of Ag@SiO$_2$ NPs. TEM images, XRD patterns and XPS survey spectra showed that Ag was present in nanocrystal form and that Ag@SiO$_2$ NPs were thoroughly mixed into the TiO$_2$ mesoporous layer. UV-vis absorption spectra demonstrated that the optical absorption capacity of mesoporous TiO$_2$ films and PSC devices can be improved with increased loading of Ag@SiO$_2$ NPs (0–0.5 wt. %), which could be attributed to the strong LSPR and scattering effects. Finally, the variation of *J-V*, IPCE and EIS between devices with different Ag@SiO$_2$ concentrations was assessed and the results indicated that the electron transporting paths were blocked by the Ag@SiO$_2$ NPs when their concentration was higher than the optimal value (0.3 wt. %). Compared to the normal PSCs (0 wt. % Ag@SiO$_2$-TiO$_2$), the PSCs incorporating the optimal content of NPs exhibited a 19.46% improvement of the PCE (from 12.23% to 14.61%) and 13.89% improvement of J_{SC} (from 20.23 mA/cm^2 to 23.04 mA/cm^2). Our method of using Ag@SiO$_2$ NPs provides a new approach to boosting highly efficient hole-conductor-free PSCs based on carbon counter electrodes.

Author Contributions: Conceptualization, B.W., X.Z., S.L. and M.C.; Data curation, B.W., X.Z., S.L. and M.C.; Investigation, B.W., X.Z., S.L. and M.C.; Methodology, B.W., X.Z., S.L. and M.C.; Software, B.W., X.Z., S.L. and M.C.; Writing-original draft, B.W., X.Z., S.L. and M.C.; Writing–review and editing, H.L. and Y.Y.

Conflicts of Interest: The authors declare no conflict of interest.

References

1. Arora, N.; Dar, M.I.; Hinderhofer, A.; Pellet, N.; Schreiber, F.; Zakeeruddin, S.M.; Grätzel, M. Perovskite solar cells with CuSCN hole extraction layers yield stabilized efficiencies greater than 20%. *Science* **2017**, *358*, 768–771. [CrossRef] [PubMed]

2. Chen, H.; Ye, F.; Tang, W.; He, J.; Yin, M.; Wang, Y.; Xie, F.; Bi, E.; Yang, X.; Grätzel, M.; et al. A solvent- and vacuum-free route to large-area perovskite films for efficient solar modules. *Nature* **2017**, *550*, 92. [CrossRef] [PubMed]

3. Kojima, A.; Teshima, K.; Shirai, Y.; Miyasaka, T. Organometal Halide Perovskites as Visible-Light Sensitizers for Photovoltaic Cells. *J. Am. Chem. Soc.* **2009**, *131*, 6050–6051. [CrossRef] [PubMed]

4. Jeon, N.J.; Na, H.; Jung, E.H.; Yang, T.Y.; Lee, Y.G.; Kim, G.; Shin, H.W.; Seok, S.I.; Lee, J.; Seo, J. A fluorene-terminated hole-transporting material for highly efficient and stable perovskite solar cells. *Nat. Energy* **2018**, *3*, 682–689. [CrossRef]

5. Green, M.A.; Hobaillie, A.; Snaith, H.J. The emergence of perovskite solar cells. *Nat. Photonics* **2014**, *8*, 506–514. [CrossRef]

6. Chen, C.W.; Hsiao, S.Y.; Chen, C.Y.; Kang, H.W.; Huang, Z.Y.; Lin, H.W. Optical Properties of Organometal Halide Perovskite Thin Films and General Device Structure Design Rules for Perovskite Single and Tandem Solar Cells. *J. Mater. Chem. A* **2014**, *3*, 9152–9159. [CrossRef]

7. Stoumpos, C.C.; Malliakas, C.D.; Kanatzidis, M.G. Semiconducting tin and lead iodide perovskites with organic cations: Phase transitions, high mobilities, and near-infrared photoluminescent properties. *Inorg. Chem.* **2013**, *52*, 9019–9038. [CrossRef] [PubMed]

8. Hu, J.; Qiao, Y.; Yang, Y.; Zhao, L.; Liu, W.; Li, S.; Liu, P.; Chen, M. Enhanced Performance of Hole-Conductor-Free Perovskite Solar Cells by Utilization of Core/Shell-Structured β-NaYF$_4$:Yb^{3+}, Er^{3+}@SiO$_2$ Nanoparticles in Ambient Air. *IEEE J. Photovolt.* **2017**, *8*, 132–136. [CrossRef]

9. Qiao, Y.; Li, S.; Liu, W.; Ran, M.; Lu, H.; Yang, Y. Recent Advances of Rare-Earth Ion Doped Luminescent Nanomaterials in Perovskite Solar Cells. *Nanomaterials* **2018**, *8*, 43. [CrossRef] [PubMed]

10. Bella, F.; Renzi, P.; Cavallo, C.; Gerbaldi, C. Caesium for perovskite solar cells: an overview. *Chem. Eur. J.* **2018**, *24*, 12183–12205. [CrossRef] [PubMed]

11. Bella, F.; Garcia, A.B.M.; Meligrana, G.; Lamberti, A.; Destro, M.; Pavone, M.; Gerbaldi, C. Unveiling the controversial mechanism of reversible Na storage in TiO$_2$ nanotube arrays: Amorphous versus anatase TiO$_2$. *Nano Res.* **2017**, *10*, 2891–2903. [CrossRef]

12. Zhang, C.; Liu, S.; Qi, Y.; Cui, F.; Yang, X. Conformal carbon coated TiO$_2$ aerogel as superior anode for lithium-ion batteries. *Chem. Eng. J.* **2018**, *351*, 825–831. [CrossRef]

13. Bella, F.; Verna, A.; Gerbaldi, C. Patterning dye-sensitized solar cell photoanodes through a polymeric approach: A perspective. *Mater. Sci. Semicond. Process.* **2018**, *73*, 92–98. [CrossRef]

14. Galliano, S.; Bella, F.; Piana, G.; Giacona, G.; Viscardi, G.; Gerbaldi, C.; Grätzel, M.; Barolo, C. Finely tuning electrolytes and photoanodes in aqueous solar cells by experimental design. *Sol. Energy* **2018**, *163*, 251–255. [CrossRef]

15. Abate, A.; Baena, J.P.C.; Saliba, M.; Suait, M.S.; Bella, F. Perovskite solar cells from the lab to the assembly line. *Chem. Eur. J.* **2018**, *24*, 3083–3100. [CrossRef] [PubMed]

16. Babayigit, A.; Ethirajan, A.; Muller, M.; Conings, B. Toxicity of organometal halide perovskite solar cells. *Nat. Mater.* **2016**, *15*, 247–251. [CrossRef] [PubMed]

17. Babayigit, A.; Thanh, D.D.; Ethirajan, A.; Manca, J.; Muller, M.; Boyen, H.G.; Conings, B. Assessing the toxicity of Pb- and Sn-based perovskite solar cells in model organism Danio rerio. *Sci. Rep.* **2016**, *6*, 18721. [CrossRef] [PubMed]

18. Huang, X.; Neretina, S.; Elsayed, M.A. Gold nanorods: from synthesis and properties to biological and biomedical applications. *Adv. Mater.* **2010**, *21*, 4880–4910. [CrossRef] [PubMed]

19. Stratakis, E.; Kymakis, E. Nanoparticle-based plasmonic organic photovoltaic devices. *Mater. Today* **2013**, *16*, 133–146. [CrossRef]

20. Petridis, C.; Savva, K.; Kymakis, E.; Stratakis, E. Laser generated nanoparticles based photovoltaics. *J. Colloid Interface Sci.* **2017**, *489*, 28–37. [CrossRef] [PubMed]

21. Kelly, K.L.; Coronado, E.; Zhao, L.L.; Schatz, G.C. The Optical Properties of Metal Nanoparticles: The Influence of Size, Shape, and Dielectric Environment. *Cheminform* **2003**, *34*, 668–677. [CrossRef]

22. Chan, K.; Wright, M.; Elumalai, N.; Uddin, A.; Pillai, S. Plasmonics in Organic and Perovskite Solar Cells: Optical and Electrical Effects. *Adv. Opt. Mater.* **2017**, *5*, 1600698. [CrossRef]

23. Choy, W.C.H. Using plasmonic-electrical effects for high-performance organic solar cells. *Spienewsroom* **2013**, *23*, 4255–4261. [CrossRef]

24. Ren, X.; Cheng, J.; Zhang, S.; Li, X.; Rao, T.; Huo, L.; Hou, J.; Choy, W.C. High Efficiency Organic Solar Cells Achieved by the Simultaneous Plasmon-Optical and Plasmon-Electrical Effects from Plasmonic Asymmetric Modes of Gold Nanostars. *Small* **2016**, *12*, 5102. [CrossRef]

25. Paci, B.; Generosi, A.; Albertini, V.R.; Spyropoulos, G.D.; Stratakis, E.; Kymakis, E. Enhancement of photo/thermal stability of organic bulk heterojunction photovoltaic devices via gold nanoparticles doping of the active layer. *Nanoscale* **2012**, *4*, 7452–7459. [CrossRef] [PubMed]

26. Wang, D.H.; Kim, D.Y.; Choi, K.W.; Seo, J.H.; Im, S.H.; Park, J.H.; Park, O.O.; Heeger, A.J. Enhancement of Donor–Acceptor Polymer Bulk Heterojunction Solar Cell Power Conversion Efficiencies by Addition of Au Nanoparticles. *Angew. Chem. Int. Ed. Engl.* **2011**, *123*, 5519–5523. [CrossRef] [PubMed]

27. Kulkarni, A.P.; Noone, K.M.; Munechika, K.; Guyer, S.R.; Ginger, D.S. Plasmon-enhanced charge carrier generation in organic photovoltaic films using silver nanoprisms. *Nano Lett.* **2010**, *10*, 1501–1505. [CrossRef] [PubMed]

28. Batmunkh, M.; Macdonald, T.J.; Peveler, W.J.; Bati, A.S.R.; Carmalt, C.J.; Parkin, I.P.; Shapter, J.G. Plasmonic Gold Nanostars Incorporated into High-Efficiency Perovskite Solar Cells. *ChemSuSChem* **2017**, *10*, 3750–3753. [CrossRef] [PubMed]

29. Wang, Y.; Zhai, J.; Song, Y.; He, L. The Ag shell thickness effect of Au@Ag@SiO$_2$ core-shell nanoparticles on the optoelectronic performance of dye sensitized solar cells. *Chem. Commun.* **2016**, *52*, 2390–2393. [CrossRef] [PubMed]

30. Jankovic, V.; Yang, Y.M.; You, J.; Dou, L.; Liu, Y.; Cheung, P.; Chang, J.P.; Yang, Y. Active layer-incorporated, spectrally tuned Au/SiO$_2$ core/shell nanorod-based light trapping for organic photovoltaics. *ACS Nano* **2013**, *7*, 3815–3822. [CrossRef] [PubMed]

31. Wu, R.; Yang, B.; Zhang, C.; Huang, Y.; Cui, Y.; Liu, P.; Zhou, C.; Hao, Y.; Gao, Y.; Yang, J. Prominent Efficiency Enhancement in Perovskite Solar Cells Employing Silica-Coated Gold Nanorods. *J. Phys. Chem. C* **2016**, *120*, 6996–7004. [CrossRef]

32. Cui, J.; Chen, C.; Han, J.; Cao, K.; Zhang, W.; Shen, Y.; Wang, M. Surface Plasmon Resonance Effect in Inverted Perovskite Solar Cells. *Adv. Sci.* **2016**, *3*, 1500312–1500320. [CrossRef] [PubMed]

33. Fan, R.; Wang, L.; Chen, Y.; Zheng, G.; Li, L.; Li, Z.; Zhou, H. Tailored Au@TiO$_2$ Nanostructures for Plasmonic Effect in Planar Perovskite Solar Cells. *J. Mater. Chem. A* **2017**, *5*, 12034–12042. [CrossRef]

34. Zhang, W.; Saliba, M.; Stranks, S.D.; Sun, Y.; Shi, X.; Wiesner, U.; Snaith, H.J. Enhancement of perovskite-based solar cells employing core-shell metal nanoparticles. *Nano Lett.* **2013**, *13*, 4505–4510. [CrossRef] [PubMed]

35. Hao, H.; Wang, L.; Ma, X.; Cao, K.; Yu, H.; Wang, M.; Gu, W.; Zhu, R.; Anwar, M.S.; Chen, S.; et al. Improved Efficiency of Inverted Perovskite Solar Cells Via Surface Plasmon Resonance Effect of Au@PSS Core–Shell Tetrahedra Nanoparticles. *Sol. RRL* **2018**, *2*, 1800061. [CrossRef]

36. Luo, Q.; Zhang, C.; Deng, S.; Zhu, H.; Li, Z.; Wang, Z.; Chen, X.; Huang, S. Plasmonic Effects of Metallic Nanoparticles on Enhancing Performance of Perovskite Solar Cells. *ACS Appl. Mater. Interfaces* **2017**, *9*, 34821–34832. [CrossRef] [PubMed]

37. Brown, M.D.; Suteewong, T.; Kumar, R.S.S.; Innocenzo, V.D.; Petrozza, A.; Lee, M.; Wiesner, U.; Snaith, H.J. Plasmonic Dye-Sensitized Solar Cells Using Core−Shell Metal−Insulator Nanoparticles. *Nano Lett.* **2011**, *11*, 438. [CrossRef] [PubMed]

38. Wang, Z.; Hao, Y.; Wang, W.; Cui, Y.; Sun, Q.; Ji, T.; Li, Z.; Wang, H.; Zhu, F. Incorporating silver-SiO$_2$ core-shell nanocubes for simultaneous broadband absorption and charge collection enhancements in organic solar cells. *Synth. Met.* **2016**, *220*, 612–620. [CrossRef]

39. Chan, K.H.; Elumalai, N.K.; Tayebjee, M.J.Y.; Uddin, A.; Pillai, S. Dark carrier dynamics and electrical characteristics of organic solar cells integrated with Ag-SiO$_2$ core-shell nanoparticles. *Synth. Met.* **2017**, *223*, 34–42. [CrossRef]

40. Baek, S.W.; Noh, J.; Lee, C.H.; Kim, B.S.; Seo, M.K.; Lee, J.Y. Plasmonic Forward Scattering Effect in Organic Solar Cells: A Powerful Optical Engineering Method. *Sci. Rep.* **2013**, *3*, 542. [CrossRef]

41. Stöber, W.; Fink, A.; Bohn, E. Controlled growth of monodisperse silica spheres in the micron size range. *J. Colloid Interface Sci.* **1968**, *26*, 62–69. [CrossRef]

42. Wang, X.; Yu, J.C.; Ho, C.; Mak, A.C. A robust three-dimensional mesoporous Ag/TiO$_2$ nanohybrid film. *Chem. Commun.* **2005**, *17*, 2262–2264. [CrossRef] [PubMed]

43. Tom, R.T.; Nair, A.S.; Singh, N.; Aslam, M.; Nagendra, C.L.; Philip, R.; Vijayamohanan, K.; Pradeep, T. Freely Dispersible Au@TiO$_2$, Au@ZrO$_2$, Ag@TiO$_2$, and Ag@ZrO$_2$ Core−Shell Nanoparticles: One-Step Synthesis, Characterization, Spectroscopy, and Optical Limiting Properties. *Langmuir* **2003**, *19*, 3439–3445. [CrossRef]

44. Choi, H.; Lee, J.P.; Ko, S.J.; Jung, J.W.; Park, H.; Yoo, S.; Park, O.; Jeong, J.R.; Park, S.; Kim, J.Y. Multipositional silica-coated silver nanoparticles for high-performance polymer solar cells. *Nano Lett.* **2013**, *13*, 2204. [CrossRef] [PubMed]

45. Jain, P.K.; El-Sayed, M.A. Noble metal nanoparticle pairs: effect of medium for enhanced nanosensing. *Nano Lett.* **2008**, *8*, 4347–4352. [CrossRef] [PubMed]

46. Bardhan, R.; Grady, N.K.; Halas, N.J. Nanoscale control of near-infrared fluorescence enhancement using Au nanoshells. *Small* **2008**, *4*, 1716–1722. [CrossRef] [PubMed]

47. Mori, K.; Kawashima, M.; Che, M.; Yamashita, H. Enhancement of the Photoinduced Oxidation Activity of a Ruthenium (II) Complex Anchored on Silica-Coated Silver Nanoparticles by Localized Surface Plasmon Resonance. *Angew. Chem. Int. Ed.* **2010**, *122*, 8780–8783. [CrossRef]

48.　Luo, K.; Clair, T.P.S.; Lai, X.; Goodman, D.W. Silver Growth on TiO$_2$(110) (1 × 1) and (1 × 2). *J. Phys. Chem. B* **2000**, *104*, 1374–1377. [CrossRef]

49.　Zarick, H.F.; Erwin, W.R.; Aufrecht, J.; Coppola, A.; Rogers, B.R.; Pint, C.L.; Bardhan, R. Morphological modulation of bimetallic nanostructures for accelerated catalysis. *J. Mater. Chem. A* **2014**, *2*, 7088–7098. [CrossRef]

50.　Mei, A.; Li, X.; Liu, L.; Ku, Z.; Liu, T.; Rong, Y.; Xu, M.; Hu, M.; Chen, J.; Yang, Y.; et al. A hole-conductor–free, fully printable mesoscopic perovskite solar cell with high stability. *Science* **2014**, *345*, 295–298. [CrossRef] [PubMed]

51.　Yue, L.; Yan, B.; Attridge, M.; Wang, Z. Light absorption in perovskite solar cell: Fundamentals and plasmonic enhancement of infrared band absorption. *Sol. Energy* **2016**, *124*, 143–152. [CrossRef]

52.　Shi, X.; Ueno, K.; Takabayashi, N.; Misawa, H. Plasmon-Enhanced Photocurrent Generation and Water Oxidation with a Gold Nanoisland-Loaded Titanium Dioxide Photoelectrode. *J. Phys. Chem. C* **2013**, *117*, 2494–2499. [CrossRef]

53.　Lee, J.E.; Bera, S.; Choi, Y.S.; Lee, W.I. Size-dependent plasmonic effects of M and M@SiO$_2$, (M = Au or Ag) deposited on TiO$_2$ in photocatalytic oxidation reactions. *Appl. Catal. B Environ.* **2017**, *214*, 15–22. [CrossRef]

54.　Zhang, Y.J. Investigation of Gold and Silver Nanoparticles on Absorption Heating and Scattering Imaging. *Plasmonics* **2011**, *6*, 393–397. [CrossRef]

55.　Li, S.; Hu, J.; Yang, Y.; Zhao, L.; Qiao, Y.; Liu, W.; Liu, P.; Chen, M. Ag/nano-TiO$_2$ composite compact film for enhanced performance of perovskite solar cells based on carbon counter electrodes. *Appl. Phys. A* **2017**, *123*, 628. [CrossRef]

56.　Gangishetty, M.K.; Lee, K.E.; Scott, R.W.; Kelly, T.L. Plasmonic Enhancement of Dye Sensitized Solar Cells in the Red-to-near-Infrared Region using Triangular Core-Shell Ag@SiO$_2$ Nanoparticles. *Appl. Mater. Interfaces* **2013**, *5*, 11044. [CrossRef] [PubMed]

57.　Nemnes, G.A.; Besleaga, C.; Tomulescu, A.G.; Pintilie, I.; Pintilie, L.; Torfason, K.; Manolescu, A. Dynamic electrical behavior of halide perovskite based solar cells. *Sol. Energy Mater. Sol. Cells* **2017**, *159*, 197–203. [CrossRef]

58.　Nemnes, G.A.; Besleaga, C.; Stancu, V.; Dogaru, D.E.; Leonat, L.N.; Pintilie, L.; Torfason, K.; Ilkov, M.; Manolescu, A. Normal and Inverted Hysteresis in Perovskite Solar Cells. *J. Phys. Chem. C* **2017**, *121*, 11207–11214. [CrossRef]

59.　Snaith, H.J.; Abate, A.; Ball, J.M.; Eperon, G.E.; Leijtens, T.; Noel, N.K.; Stranks, S.D.; Wang, J.T.W.; Wojciechowski, K.; Zhang, W. Anomalous Hysteresis in Perovskite Solar Cells. *J. Phys. Chem. Lett.* **2014**, *5*, 1511–1515. [CrossRef] [PubMed]

60.　Rong, Y.; Hu, Y.; Ravishankar, S.; Liu, H.; Hou, X.; Sheng, Y.; Mei, A.; Wang, Q.; Li, D.; Xu, M.; et al. Tunable hysteresis effect for perovskite solar cells. *Energy Environ. Sci.* **2017**, *10*, 2383–2391. [CrossRef]

61.　Kakavelakis, G.; Petridis, K.; Kymskis, E. Recent advances in plasmonic metal and rare-earth-element upconversion nanoparticle doped perovskite solar cells. *J. Mater. Chem. A* **2017**, *5*, 21604–21624. [CrossRef]

62.　Li, S.; Zhu, X.; Wang, B.; Qiao, Y.; Liu, W.; Yang, H.; Liu, N.; Chen, M.; Lu, H.; Yang, Y. Influence of Ag Nanoparticles with Different Sizes and Concentrations Embedded in a TiO$_2$ Compact Layer on the Conversion Efficiency of Perovskite Solar Cells. *Nanoscale Res. Lett.* **2018**, *13*, 210. [CrossRef] [PubMed]

63.　Kang, S.H.; Choi, S.H.; Kang, M.S.; Kim, J.Y.; Kim, S.H.; Hyeon, T.; Sung, Y.E. Nanorod-Based Dye-Sensitized Solar Cells with Improved Charge Collection Efficiency. *Adv. Mater.* **2008**, *20*, 54–58. [CrossRef]

64.　Ghadiri, E.; Taghavinia, N.; Zakeeruddin, S.M.; Gratzel, M.; Moser, J.E. Enhanced electron collection efficiency in dye-sensitized solar cells based on nanostructured TiO$_2$ hollow fibers. *Nano Lett.* **2010**, *10*, 1632–1638. [CrossRef] [PubMed]

65.　Wang, Y.; Zhou, X.; Liang, C.; Li, P.; Hu, X.; Cai, Q.; Zhang, Y.; Li, F.; Li, M.; Song, Y. Enhanced Effciency of Perovskite Solar Cells by using Core–Ultrathin Shell Structure Ag@SiO2 Nanowires as Plasmonic Antennas. *Adv. Electron. Mater.* **2017**, *3*, 1700169. [CrossRef]

66.　Perez, E.J.J.; Wuβler, M.; Santiago, F.F.; Wollny, K.L.; Mankel, E.; Mayer, T.; Jaegermann, W.; Sero, I.M. Role of the selective contacts in the performance of lead halide perovskite solar cells. *J. Phys. Chem. Lett.* **2014**, *5*, 680–685. [CrossRef] [PubMed]

67.　Rong, Y.; Ku, Z.; Mei, A.; Liu, T.; Xu, M.; Ko, S.; Li, X.; Han, H. Hole-conductor-free mesoscopic TiO$_2$/CH$_3$NH$_3$PbI$_3$ heterojunction solar cells based on anatase nanosheets and carbon counter electrodes. *J. Phys. Chem. Lett.* **2014**, *5*, 2160–2164. [CrossRef] [PubMed]

68. Gao, X.; Li, J.; Baker, J.; Hou, Y.; Guan, D.; Chen, J.; Yuan, C. Enhanced photovoltaic performance of perovskite CH$_3$NH$_3$PbI$_3$ solar cells with freestanding TiO$_2$ nanotube array films. *Chem. Commun. (Camb.)* **2014**, *50*, 6368–6371. [CrossRef] [PubMed]

69. Zhao, T.; Sun, R.; Yu, S.; Zhang, Z.; Zhou, L.; Huang, H.; Du, R. Size-controlled preparation of silver nanoparticles by a modified polyol method. *Colloid Surf. A* **2010**, *366*, 197–202. [CrossRef]

70. Saliba, M.; Zhang, W.; Burlakov, V.M.; Stranks, S.D.; Sun, Y.; Ball, J.M.; Johnston, M.B.; Goriely, A.; Wiesner, U.; Snaith, H.J. Plasmonic-Induced Photon Recycling in Metal Halide Perovskite Solar Cells. *Adv. Funct. Mater.* **2015**, *25*, 5038–5046. [CrossRef]

71. Bai, Z.; Chen, R.; Si, P.; Huang, Y.; Sun, H.; Kim, D.H. Fluorescent pH sensor based on Ag@SiO$_2$ core-shell nanoparticle. *ACS Appl. Mater. Interfaces* **2013**, *5*, 5856–5860. [CrossRef] [PubMed]